Nonlinear Multiscale Regularisation in MR Elastography: Towards Fine Feature Mapping

Accepted Manuscript

Nonlinear Multiscale Regularisation in MR Elastography: Towards Fine Feature Mapping

Eric Barnhill, Lyam Hollis, Ingolf Sack, Jürgen Braun,
Peter R. Hoskins, Pankaj Pankaj, Colin Brown, Edwin J.R. van Beek,
Neil Roberts

Please cite this article as: Eric Barnhill, Lyam Hollis, Ingolf Sack, Jürgen Braun, Peter R. Hoskins, Pankaj Pankaj, Colin Brown, Edwin J.R. van Beek, Neil Roberts, Nonlinear Multiscale Regularisation in MR Elastography: Towards Fine Feature Mapping, *Medical Image Analysis* (2016), doi: 10.1016/j.media.2016.05.012

Highlights

- New Magnetic Resonance Elastography (MRE) software pipeline incorporating wavelet-based denoising and feature-detection techniques

- Systematic noise testing with new Finite Element Method (FEM)–based simulations

- Results robust to noise and show new levels of detail for MRE elastograms

MRE Acquisition Magnitude
(Anatomical)
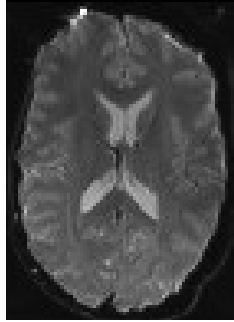
MRE Acquisition Phase
(Shear Wave Motion)
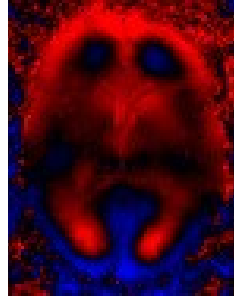
Heterogeneous
viscoelasticity
maps
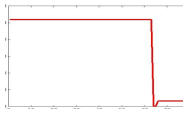
Wave inversion w/ feature detection
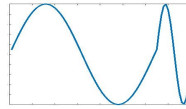
Sparse noise filter
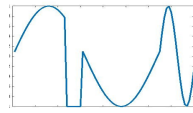
High frequency noise filter
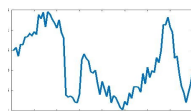
Low freq. noise filter
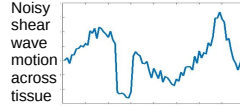
Noisy
shear
wave
motion
across
tissue

Elasticity Map
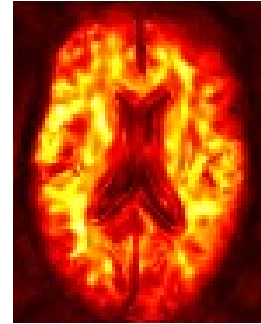
Viscosity Map
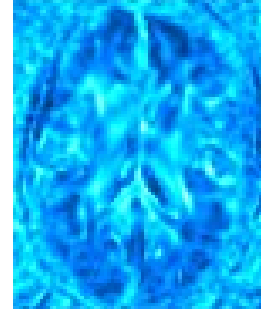
Nonlinear Multiscale Regularisation in MR Elastography: Towards Fine Feature Mapping

Eric Barnhill[a,∗], Lyam Hollis[b], Ingolf Sack[c], Jürgen Braun[c], Peter R Hoskins[b], Pankaj Pankaj[d], Colin Brown[e], Edwin J R van Beek[a], Neil Roberts[a]

[a]*Clinical Research Imaging Centre, College of Medicine and Veterinary Medicine, The University of Edinburgh, Edinburgh, UK EH16 4TJ*
[b]*BHF Centre for Cardiovascular Science, College of Medicine and Veterinary Medicine, The University of Edinburgh, Edinburgh, YK, EH16 4TJ*
[c]*Charité Universitätsmedizin Berlin, Charitéplatz 1, 10117, Berlin, Germany*
[d]*School of Engineering, University of Edinburgh, King's Buildings, Mayfield Road, Edinburgh, EH9 3JL*
[e]*Research and Development, The Mentholatum Company, East Kilbride, UK G74 5PE*

Abstract

Fine-featured elastograms may provide additional information of radiological interest in the context of *in vivo* elastography. Here a new image processing pipeline called ESP (Elastography Software Pipeline) is developed to create Magnetic Resonance Elastography (MRE) maps of viscoelastic parameters (complex modulus magnitude $|G^*|$ and loss angle ϕ) that preserve fine-scale information through nonlinear, multi-scale extensions of typical MRE post-processing techniques. **Methods:** A new MRE image processing pipeline was developed that incorporates wavelet-domain denoising, image-driven noise estimation, and feature detection. ESP was first validated using simulated data, including viscoelastic Finite Element Method (FEM) simulations, at multiple noise levels. ESP images were compared with MDEV pipeline images, both in the FEM models and in three ten-subject cohorts of brain, thigh, and liver acquisitions. ESP and MDEV mean values were compared to 2D LFE mean values for the same cohorts as a benchmark. Finally the proportion of spectral

---

[∗]Corresponding author
Email addresses: `e.barnhill@sms.ed.ac.uk` (Eric Barnhill),
`s1160274@staffmail.ed.ac.uk` (Lyam Hollis), `ingolf.sack@charite.de` (Ingolf Sack),
`juergen.braun@charite.de` (Jürgen Braun), `Peter.Hoskins@ed.ac.uk` (Peter R Hoskins),
`Pankaj@ed.ac.uk` (Pankaj Pankaj), `brown@mentholatum.co.uk` (Colin Brown),
`edwin-vanbeek@ed.ac.uk` (Edwin J R van Beek), `neil.roberts@ed.ac.uk` (Neil Roberts)

energy at fine frequencies was quantified using the Reduced Energy Ratio (RER) for both ESP and MDEV. ***Results:*** Blind estimates of added noise (σ) were within $5.3\% \pm 2.6\%$ of prescribed, and the same technique estimated σ in the *in vivo* cohorts at $1.7 \pm 0.8\%$. A $5 \times 5 \times 5$ truncated Gabor filter bank effectively detects local spatial frequencies at wavelengths $\lambda \leq 10px$. For FEM inversions, mean $|G^*|$ of hard target, soft target, and background remained within 8% of prescribed up to $\sigma = 20\%$, and mean ϕ results were within 10%, excepting hard target ϕ, which required redrawing around a ring artefact to achieve similar accuracy. Inspection of FEM $|G^*|$ images showed some spatial distortion around hard target boundaries and inspection of ϕ images showed ring artefacts around the same target. For the *in vivo* cohorts, ESP results showed mean correlation of $\mathbf{R} = 0.83$ with MDEV and liver stiffness estimates within 7% of 2D-LFE results. Finally, ESP showed statistically significant increase in fine feature spectral energy as measured with RER for both $|G^*|$ ($p < 1 \times 10^{-9}$) and ϕ ($p < 1 \times 10^{-3}$). ***Conclusion:*** Information at finer frequencies can be recovered in ESP elastograms in typical experimental conditions, however scatter- and boundary-related artefacts may cause the fine features to have inaccurate values. In *in vivo* cohorts, ESP delivers an increase in fine feature spectral energy, and better performance with longer wavelengths, than MDEV while showing similar stability and robustness.

Keywords: elastography, magnetic resonance elastography, wave inversion, complex dualtree wavelet, denoising

---

1. Introduction

In the present study a new post-processing pipeline for the Magnetic Resonance Elastography (MRE) inversion problem, known as the Elastography Software Pipeline (ESP), was developed to enable fine-featured dual-parameter elasticity map reconstruction. Soft tissue viscoelastic parameters are valuable diagnostic tools, and more finely featured viscoelastic property mapping would deliver additional information about the tissue under study that may be of

4

radiological interest.

Magnetic Resonance Elastography (MRE) (Muthupillai et al., 1995) uses phase-contrast MRI imaging to measure tissue viscoelastic properties *in vivo*. In a typical MRE experiment, steady-state wave propagation is induced in tissue using an external driver, and wave inversion is used to measure viscoelastic properties. The most commonly reported result is a measure of tissue stiffness or elasticity, and some studies also report a second parameter of viscous dispersion. Here the magnitude of the complex shear modulus $|G^*|$ is reported as a stiffness estimate, and phase angle of the complex modulus ϕ is reported as a viscosity estimate. While phase angle technically measures the relationship between storage and loss moduli of the tissue, ϕ is commonly used as a viscosity measure since a value of 0 reflects a material with no viscosity, and a value of $\frac{\pi}{2}$ reflects a purely viscous material (Malkin and Isayev, 2006).

Increasing MRE resolution to map fine features in two parameters may enable new applications for non-invasive tissue analysis based on viscoelastic property measurements. For example, the diffuse mechanical parameter alterations found in certain brain diseases (Sack et al., 2013) can be mapped to regions of white or gray matter; or alterations in limb behaviour can be mapped to changes in specific intra-muscle structures (Barnhill et al., 2013). However, rheological methods determine viscoelastic properties through wave inversion which is highly ill-posed and sensitive to noise (Aster et al., 2013). MRE is well described by a mixed dense-sparse noise model, as it contains dense high and low frequency noise common to image processing (Bertero and Boccacci, 2010), as well as frequency-dependent sparse noise arising from the complexities of shear wave propagation in complex-boundaried materials. As the first type of noise is stochastic while the second is structured and reproducible, such a pipeline must combine varied techniques to address these noise sources without sacrifice of bandwidth.

In the MRE literature a wide variety of filtering approaches are taken to reduce noise, including bandpass or other frequency-domain filtering (Klatt et al., 2007; Manduca et al., 2003; Green et al., 2008; Honarvar et al., 2012; Park

5

and Maniatty, 2006; McGarry, 2013), and derivative-fitting approaches such as binomial filtering (Sinkus et al., 2000) or Savitsky-Golay filtering (Manduca et al., 2001). All these filtering approaches require *a priori* windowing, which restricts results to features within a specified bandwidth. Recovery of the finest features, however, requires preservation of the full bandwidth range. This can be attained by multi-scale, non-linear denoising techniques including wavelet shrinkage (Donoho and Johnstone, 1995; Selesnick et al., 2005) and sparse approximation (Aharon et al., 2006; Chen and Selesnick, 2014).

The Elastography Software Pipeline (ESP) was developed to apply such techniques to preserve fine feature information in elastograms, with the aim of fine feature mechanical property recovery. ESP accomplishes this with three steps:

- Denoising is performed in wavelet bases using shrinkage and sparsity promotion;

- Noise is estimated using adaptive, image-driven measurements;

- Multi-scale feature detection is incorporated into Helmholtz inversion using a bank of truncated Gabor filters.

The new features in the pipeline were tested with analytic and Finite Element Method (FEM) data at varying noise levels and the pipeline was then applied to ten-subject cohorts of brain, liver, and thigh muscle.

2. Methods

2.1. Pipeline

2.1.1. Overview

ESP first phase unwraps the data using a 4D Laplacian-based algorithm described in Barnhill et al. (2014). ESP then applies two denoising methods not previously applied to MRE: a divergence-free-wavelet Hodge decomposition with

6

	Noise Type	Noise Removal Technique	Thresholding / Weighting Criterion	Noise Estimation Criterion
1	Phase Wrap	Laplacian-Based Unwrap[1]	N/A	N/A
2	Low-frequency dense noise	Divergence-Free Wavelet (DFW) Decomposition[2]	SureShrink[5]	Median Absolute Deviation[7]
3	High-frequency dense noise	Complex Dual-Tree Wavelet (CDTW) Denoise[3]	Overlapping Group Sparsity (OGS)[6]	Principal Component Analysis (PCA) patch-based noise estimate[8]
4	Structured noise from wave motion	MDEV inversion[4]	Magnitude of complex Gabor filter bank response	N/A

[1] Barnhill et al 2014 [2] Ong et al. 2014 [3] Selesnick et al 2005 [4] Papazoglou et al 2012 [5] Donoho et al 1995
[6] Chen & Selesnick 2013 [7] Donoho & Huber 1983 [8] Liu et al 2013

Figure 1: Summary of noise removal steps in the ESP pipeline.

SureShrink thresholding (Ong et al., 2014), and a complex dual-tree wavelet denoising (Selesnick et al., 2005) with Overlapping Group Sparsity (OGS) thresholding (Chen and Selesnick, 2014). For handling sparse noise, ESP then applies an overdetermination-based method from the MRE literature known as the MDEV equations (Papazoglou et al., 2012). However, ESP applies a newly designed filter bank to extend the MDEV equations so that local directional spatial frequency information is used to weight the inversion at each voxel. ESP's methodological components are summarised in Figure 1 and described in more detail below. Noise standard deviation is described below as % of maximum signal.

2.1.2. Removal of low frequency dense noise (e.g. bulk waves)

MRE possesses several slowly-varying noise sources, including phase field biases, rigid body motion, and bulk wave motion: as soft tissue is not fully incompressible, shear vibration of tissue also produces bulk waves which are an order of magnitude longer than shear waves. Bulk waves have been shown to impact shear wave measurements and therefore cannot be neglected (Sinkus et al., 2000). Techniques used to handle bulk waves in other studies include

7

high-pass filtering (Klatt et al., 2010; McGarry, 2013) or the inversion of x and y gradients (Hirsch et al., 2014). As bulk waves are divergent, one common technique is application of a Helmholtz-Hodge decomposition (HHD) to the MRE acquisition with retention of only the rotational component (Sinkus et al., 2005a; Honarvar et al., 2013). However, from a signal processing standpoint, the implementation of an HHD to heterogeneous data is not straightforward as sharp edges such as anatomical boundaries will have high divergence and errors will propagate through the image (Ong et al., 2014).

In ESP a 3D divergence-free wavelet (Ong et al., 2014) is applied to eliminate dense low-frequency noise. The technique makes use of the contrast between the large, sparse divergence coefficients of edges and the small, dense divergence coefficients of low frequency noise sources such as bulk waves and rigid body motion, thresholding the non-divergence free coefficients to suppress small values and retain large ones. Image noise is estimated with median absolute deviation (MAD) and thresholds are determined with SureShrink (Donoho and Johnstone, 1995). For validation, analysis and comparison with similar denoising algorithms, we refer the reader to Ong et al. (2014).

2.1.3. Removal of high frequency dense noise (e.g. sensor noise)

Correct high-frequency denoising is critical to avoid parameter overestimation from oversmoothing, parameter underestimation from insufficient noise removal, and feature loss in both cases. The features to be denoised span all scales of the image and extend in arbitrary directions within the 3D volumetric space. In ESP, images are denoised using a 3D complex dual-tree wavelet (CDTW) transform (Selesnick et al., 2005). The CDTW is reported to be "an optimal representation"(Selesnick et al., 2005) for piecewise-smooth functions with discontinuities. As a fine-feature elastogram must contain data about both smooth wave propagation through homogeneous regions, and wave discontinuities at tissue interfaces, ESP denoises data in the CDTW domain.

MRE images contain phase noise which scales negatively with the magnitude of the tissue displacement. Consequently SNR levels will be different in different

image regions, depending on such factors as wave penetration. We handle this complexity with a de-noising technique new to MRE, in which sparsity is enforced among overlapping groups at multiple scales, a technique known as Overlapping Group Sparsity (OGS)(Chen and Selesnick, 2014) shrinkage. Group size controls resolution, which we here set to the edge size of the compact Laplacian operator, 3px, used in the wave inversion, using 3px as an effective minimum window for both. OGS then requires calibration of one variable, a sparsity enforcement parameter λ. More details are found in Chen and Selesnick (2014) including recommendations for setting the relation between λ and an image noise estimate σ. However Chen and Selesnick (2014) does not address the 3D case for which the ESP pipeline is the first published application. Consequently, herein we add our own calibration described in Experiments. We apply OGS separately along the Z axis and in the XY plane, as the noise profile along the Z axis can be quite different due to interslice phase discontinuities (Murphy et al., 2012). Image noise σ is estimated with a Principal Component Analysis (PCA) patch-based single image blind noise estimation technique (Liu et al., 2013) and this result is used to set the OGS sparsity enforcement term. A calibration test was used to determine a relationship between detected noise level σ and sparsity enforcement term λ expected to de-noise the image below a value of $\sigma = 0.05\%$, and this is described below in Experiments. However, otherwise our procedure is identical to Chen and Selesnick (2014) in all respects and that paper can be consulted for algorithm comparison and sensitivity analysis.

λ is not a hard or soft threshold, but is used to separate high and low magnitude coefficients after the sparsification of the overlapping groups. Given the findings of basis optimality reported in Selesnick et al. (2005) and the OGS analysis found in Chen and Selesnick (2014), the technique can be expected to provide adaptive denoising for a range of noise levels in the image.

2.1.4. Removal of sparse noise / clutter (e.g. low signal areas from standing wave nodes)

The propagation of acoustic waves through complex-boundaried soft tissue produces several sources of noise such as standing wave nodes, wave scattering and mode conversion. (While these noise sources result from violation of the assumptions of the Helmholtz inversion, rather than sensor noise, they still fit the standard signal processing definition of noise as unwanted signal.) These noise sources are irregularly placed and sparse in the input. Further, as their location is frequency-dependent, they will be highly sparse in an acquisition overdetermined at multiple frequencies. The MDEV equations, first described in Papazoglou et al. (2012), extend the Algebraic Helmholtz Inversion (AHI) or Direct Inversion (DI) approach (Papazoglou et al., 2005; Manduca et al., 2001). AHI uses simplifying assumptions of isotropy and local homogeneity to determine the complex shear modulus G^* of a Fourier-transformed wave field $U(x, y, z)$. MDEV resolves sparse noise in AHI by overdetermination, pixel-wise averaging the complex modulus magnitude $|G^*|$ and loss angle ϕ across frequencies in a multi-frequency acquisition. (Other approaches to MRE inversion that include multi-frequency based overdetermination can be found in Klatt et al. (2007) and Honarvar et al. (2013)).

As tissue shear modulus values show frequency-dependence following a power law (Szabo, 1995), the combining of the $|G^*|$ results at various frequencies is a source of error. MDEV accepts this error for the benefits of over-determining the tissue displacement matrix prior to inversion, which allows for the resolution of wave-related noise without sacrifice of bandwidth. Such error is not present in the ϕ calculation which is, per the springpot model, expected to remain constant at all frequencies (Sinkus et al., 2005b).

2.1.5. Multi-Scale Feature Detection / Gabor-Weighted Inversion

AHI and MDEV require estimation of the Laplacian and, as in the denoising techniques above, the estimator will favour particular frequencies if the estimation window is kept fixed. Here the scale of the inversion is made responsive

10

to the features in the image through incorporation of Gabor filter bank results into the MDEV equations.

Complex Gabor filters are effective multi-scale feature detectors (Gonzalez and Woods, 2002): similarity between image wavelength λ and Gabor filter tuning ϕ results in a high magnitude response when the two images are convolved, while λ more distant from ϕ results in a lower magnitude response. A Gabor filter combines a particular spatial frequency with directional smoothing appropriate to that frequency, and this provides the needed components for a Gabor Weighted Inversion (GWI). In the GWI, the image is convolved with each filter in the bank; the magnitude response is used as a voxel-wise weighting; and the directionally smoothed image, along with its Laplacian, are incorporated into the inversion equations, weighted by magnitude response at each voxel.

The weighting ensures that the inversion is not simply the average of differently smoothed images: each voxel will have high response to the filters that detect spatial frequencies at that location, and low response to the other filters. If this response is used as a weight, each voxel will effectively be inverted at its appropriate scale and not at other scales.

This result can be accomplished by extending the MDEV equations to incorporate the directionally smoothed images, the directionally smoothed Laplacians, and the voxel-wise weighting for each. For example, inversion of an acquisition of four frequencies with 3D displacements would previously have combined $4 \times 3 = 12$ results using the MDEV equations. However if the Gabor bank contains 64 filters the inversion now combines 12×64 results using the MDEV equations. The MDEV $|G^*|$ equation (4a in Braun et al. (2013)) thus expands to

$$|G^*| = \rho \frac{\sum_{m=1}^{3} \sum_{n=1}^{N} \sum_{\Phi=-\frac{\pi}{2}}^{\frac{\pi}{2}} \sum_{\theta=-\frac{\pi}{2}}^{\frac{\pi}{2}} \sum_{\nu=1}^{\frac{d}{2}} \omega_n^2 |\hat{u}_{mn\phi\theta\nu}^*(\omega_n)| \mathbf{w}_{mn\phi\theta\nu}}{\sum_{m=1}^{3} \sum_{n=1}^{N} \sum_{\Phi=-\frac{\pi}{2}}^{\frac{\pi}{2}} \sum_{\theta=-\frac{\pi}{2}}^{\frac{\pi}{2}} \sum_{\nu=1}^{\frac{d}{2}} |\nabla^2 \hat{u}_{mn\phi\theta\nu}^*(\omega_n)| \mathbf{w}_{mn\phi\theta\nu}} \quad (1)$$

with Φ pitch, θ yaw, and ν the bandwidth of the directional smoothing, $\hat{u}$ the directionally smoothed complex wavefield, $\nabla^2 \hat{u}$ the Laplacian of this field,

11

and **w** the corresponding voxel wise Gabor magnitude weighting. Similarly the equation for ϕ (4b in the same paper) expands to:

$$\phi = acos\left(-\frac{\sum_m \sum_n \sum_\Phi \sum_\theta \sum_\nu \left[\Re(\hat{u}_m)\Re(\nabla^2 \hat{u}_{mn\phi\theta\nu}) + \Im(u_{mn\phi\theta\nu})\Im(\nabla^2 \hat{u}_{mn\phi\theta\nu}) \right] w_{mn\phi\theta\nu}}{\sum_m \sum_n \sum_\Phi \sum_\theta \sum_\nu |\hat{u}^*_{mn\phi\theta\nu}(\omega_n)||\nabla^2 \hat{u}^*_{mn\phi\theta\nu}(\omega_n)|w_{mn\phi\theta\nu}} \right) \quad (2)$$

The drawback to this approach is that estimation of large wavelengths λ typically requires a Gabor filter with wide support. The GWI strikes a balance between these concerns by truncating the Gabor filters. This trade-off reduces the ability of the filter to differentiate large λ, but increases the spatial resolution of the inversion. As the interest of the paper is in the development of fine-featured elastograms, a truncated filter bank was designed to aid detection and inversion of the desired finer features, without underweighting coarse features. The appropriate truncation level, and filter bank size, for the goals of the pipeline is determined in an experiment described in Section 2.3 below.

In the filter bank, smoothing along the filter's major axis is set at the "optimal" $\sigma = \frac{2}{3}\theta$, with σ the Gaussian kernel and θ the cosine function bandwidth (Clausi and Jernigan, 2000). Minor axis support was set at $\sigma = 0.65px$, effectively setting a support of one pixel along both minor axes to maximise fineness of feature detection along the major axis (Gonzalez and Woods, 2002). As the minor axes were symmetric, roll was left stationary; as the magnitude of the response was retained, phase offset was left at zero.

2.2. Acquisitions

FEM simulations were used to verify accuracy of the ESP parameter recovery, including stiffness values of elastogram regions, and robustness to noise. Following testing, the pipeline was applied to three *in vivo* cohorts.

Finite Element Simulations Finite Element Method simulations (Thomas-Seale et al., 2011) within the ABAQUS software package (Simulia Corp., Providence, Rhode Island, USA) were used to verify the accuracy of ESP's parameter recovery in varied noise conditions. The model was designed

12

with background material of 3200 Pa stiffness, one soft target at 1600 Pa, and one hard target at 7200 Pa. The material was modelled as a Voigt solid, $G^* = \mu + i\omega\eta$, with η of $1\ Pa \cdot s$, and the solid was vibrated at four frequencies, 50, 60, 70, and 80 Hz, for an expected averaged loss modulus of 408 Pa. This produced expected $|G^*|$ of 3226 Pa, 1651 Pa and 7211 Pa for the background and two inclusions respectively and expected ϕ of 0.127, 0.250, and 0.057 radians respectively. These stiffness values were first verified with caliper measurements at all frequencies using the caliper-based wave measurement technique in e.g. Bensamoun et al. (2007) and Barnhill et al. (2013).

***In Vivo* cohorts** Three cohorts of healthy volunteers were analysed with ESP. All acquisitions were axial:

1. A cohort of ten healthy volunteer abdomens, full field MRE acquisitions, vibrated at seven frequencies (30:5:60 Hz), using a single-shot SE-EPI sequence with FoV of $320 \times 260mm^2$, ten slices, and isotropic $2.5mm^3$ voxels on a 1.5T scanner (Magnetom Sonata; Siemens Erlangen, Germany) with piezoelectric actuator and acquisition details as described in Guo et al. (2014).

2. A cohort of ten healthy volunteer brains, full field MRE acquisitions, vibrated at seven frequencies (30:5:60 Hz), using a single-shot SE-EPI sequence with FoV of $176 \times 192mm^2$, 15 slices, and isotropic $1.9mm^3$ voxels on a 3T scanner (Trio, Siemens, Erlangen, Germany) with a head cradle actuator and acquisition details as described in Guo et al. (2013).

3. A cohort of ten healthy volunteer thigh muscles, full field MRE acquisitions, vibrated at four frequencies (25:12.5:62.5 Hz) SE-EPI sequence on a 3T scanner (Verio, Siemens, Erlangen, Germany) with FoV of $336 \times 336mm^2$, 5 slices, and isotropic $3mm^3$ voxels using a ring actuator as described in Barnhill et al. (2013).

All acquisitions were approved by the relevant ethics boards.

13

2.3. Experiments

Noise detection and testing To evaluate noise detection and denoising techniques, three experiments were performed. Using the FEM simulation set described above, image noise σ was progressively added from 0 to 10% using the MATLAB (Mathworks, Natick, MA) `randn` function. Then:

- In order to establish the accuracy of the PCA noise detection in the context of MRE, the PCA-based noise detection technique was applied to estimate the σ of the simulated MRE data.

- PCA noise detection was then applied to the three acquisition cohorts described above, to estimate *in vivo* σ.

- Finally, images were denoised using different levels of the OGS sparsity enforcement parameter λ to evaluate the lowest λ that reduces noise to $\leq 0.05\%$, for the σ levels detected in the cohorts.

Truncated Gabor filter frequency detection test To investigate the frequency detection capacity of truncated Gabor filters, 1D spatial frequency data with λ ranging from 1 to 32px were convolved with 1D complex Gabor filters with tunings ϕ from 1 to 32 px, truncated to several different sizes. The responses were used to choose a truncated support size for the bank. A cut-off frequency also had to be chosen for the bank so that cumulatively for the bank, there was equal total response to all frequencies, to avoid specific frequencies being over-weighted in the inversion.

Comparative inversion of FEM simulations with added noise The FEM simulated wave images were inverted at six different Gaussian noise levels: 0, 1, 2, 3, 5, 10 and 20 percent. (Including 20% resulted in a noise level range of 46 to 16 dB which is comparable to a high-impact denoising paper such as Dabov et al. (2009) in which a range of 35-17 dB was used.) The volumes were manually segmented into soft target, hard target, and background using the original simulation settings. The ROIs were measured

14

for mean and standard deviation in $|G^*|$ and ϕ at each noise level, and the images were inspected for retention of fineness of target boundaries.

ESP results were compared with a previously published multi-frequency analysis pipeline. Here it is useful to make a distinction between the MDEV *equations*, which are used and extended in ESP, and the MDEV *method*, an inversion pipeline that uses alternate phase unwrapping and denoising techniques. In the present study ESP is compared with the MDEV method as described in Streitberger et al. (2014), which combines a gradient-based phase unwrap, 4th order Butterworth low-pass filter, and unweighted averaging of frequencies and components in the MDEV equations. Both methods are used to invert the FEM simulations at the six noise levels.

Comparison of *in vivo* cohorts The FEM results were followed with qualitative and quantitative comparisons of both inversion pipelines with *in vivo* acquisitions. The qualitative approach is presentation and inspection of images: an exemplar image is presented and discussed in terms of features of interest. Then two quantitative comparisons are made. The first is calculation of means and standard deviations, discussed more in the next section. Second is a quantitative evaluation of the proportion of image spectral energy at finer frequencies, the Reduced Energy Ratio (RER) (Lee et al., 2009), commonly used as a metric of image sharpness in computational photography. RER quantifies image sharpness by measuring the ratio of selected (i.e. reduced) higher frequency bands to the DC value of a discrete cosine transform (DCT) within 8×8 overlapping blocks. Here we extend the procedure of (Lee et al., 2009) to three dimensions due to the volumetric nature of the image, but retaining the suggested frequency bands in that paper, using frequencies above the DC but within radius 5 as the critical band. We refer the reader to (Lee et al., 2009) for further discussion of the method including robustness and sensitivity analysis. Finally as the method operates on $8 \times 8 \times 8$ blocks, the

15

values at boundaries were unreliable. Consequently RER was calculated by manually masking the images 8 voxels away from external (skull for brain, air for thigh muscle, other organs for liver) and internal (ventricles for brain, bone for thigh muscle) boundaries.

Cohort comparison of mean values of ESP, MDEV and LFE methods

We also compare mean values of ESP and MDEV results with mean values of results using the LFE method (Manduca et al., 2001; Knutsson et al., 1994) as made available in the MRE-WAVE (Mayo Clinic, Rochester, MN, USA) software package. LFE is widely used and is a useful benchmark for range and stability of ESP results. However, LFE operates on single-frequency data, and requires manually verified masking as well as several manual settings. Consequently a full comparison of pipeline results is outside the scope of this paper and we only use summary statistics of the results as a benchmark. For LFE, 3D (i.e. full-field) displacements were unwrapped with a minimum-discontinuity algorithm, filtered with a 4th order Butterworth bandpass filter with default cutoffs (2.5 and 40 waves/FOV), and inverted with 2D LFE. As LFE is single frequency, the 50Hz acquisition was used in all cases. As LFE produces no ϕ image, only ESP and MDEV were compared for ϕ results. Finally, it should be noted that LFE stiffness more closely approximates $|G^*|$ when G" is low, but diverges as G" increases. The manual masks generated with MRE-WAVE were used to mask the elastograms in all three pipelines, and mean value and standard deviation for each subject in each pipeline was measured.

3. Results

3.1. Blind Noise Estimation

Figure 2 shows results for the three de-noising experiments. In panel (a), estimated σ differs by 5.3% $\pm$ 2.6% from actual added σ. In panel (b), the same method is then used to measure the noise of the *in vivo* cohorts. *In vivo* image noise is estimated at $1.7 \pm 0.8\%$, suggesting that resolution similar to the

16

FEM 2% test case will be present in *in vivo* acquisitions. Finally, the FEM simulation images have noise added, then are de-noised with varying levels of the OGS sparsity enforcement parameter λ. As shown in panel (c), at values of $\approx 2\%$, that is to say, the estimated noise levels of the cohort, the image is effectively de-noised, that is to say, noise levels are reduced to $< 0.05\%$, when $\lambda = 0.3\sigma$.

3.2. GWI Frequency Detection

Figure 3 shows the set of 1D vectors at stepped wavelengths λ of 1 to 32 px, as well as the magnitude of the Gabor response to each wavelength from a bank of Gabor filters with tunings θ of 1 to 32 px. The Gabor response graph for 'full' shows the response of fully-supported filters, here set to a support of 3 standard deviations. The maximum response values are on the diagonal of the graph. This shows the expected result, that is, data at wavelength λ produced the highest response in filters where tuning $\theta = \lambda$.

As the bank is progressively truncated in panels (c-f), the bank still differentiates finer λ, but the response of the bank to coarser λ becomes more uniform. The result is a trade-off between support size (with a larger support combining a larger region of values, limiting image resolution) and sufficient scaling for coarse wavelengths. For the FEM and *in vivo* cohorts, a $5 \times 5 \times 5$ truncation, enabling appropriately scaled inversion of features $\lambda \leq 10px$, was chosen.

As the $5 \times 5 \times 5$ truncated bank produces a uniform weighting for $\lambda \geq 10px$ when $\theta \geq 10px$, coarser λ will be overweighted unless a cut-off θ was chosen for the bank that produced equal total Gabor magnitude response for each λ. This was done by looking at the cumulative filter bank response as larger θ filters are added to the bank, and the results are shown in Figure 4. The cut-off θ that produced the most similar total magnitude response, for the whole inversion, at all λ, was $12px$ as seen in panel (b). Since the kernels in the bank needed to be of odd dimensions, the final bank consisted of $5 \times 5 \times 5$ truncated Gabor filters with support sizes [3, 5, 7, 9, 11].

17

Estimation Of Added Noise

Estimation of Cohort Noise

(a)

(b)

Calibration Of Sparsity Enforcement Parameter (λ) For OGS Denoising Of Cohorts

(c)

Added Noise (σ)

Images in the cohorts effectively denoised at $\lambda = 0.3\sigma$

Remaining noise (est. σ) after denoising at level λ

Estimated σ in the cohorts (1.7% +/- 0.8%)

λ / σ

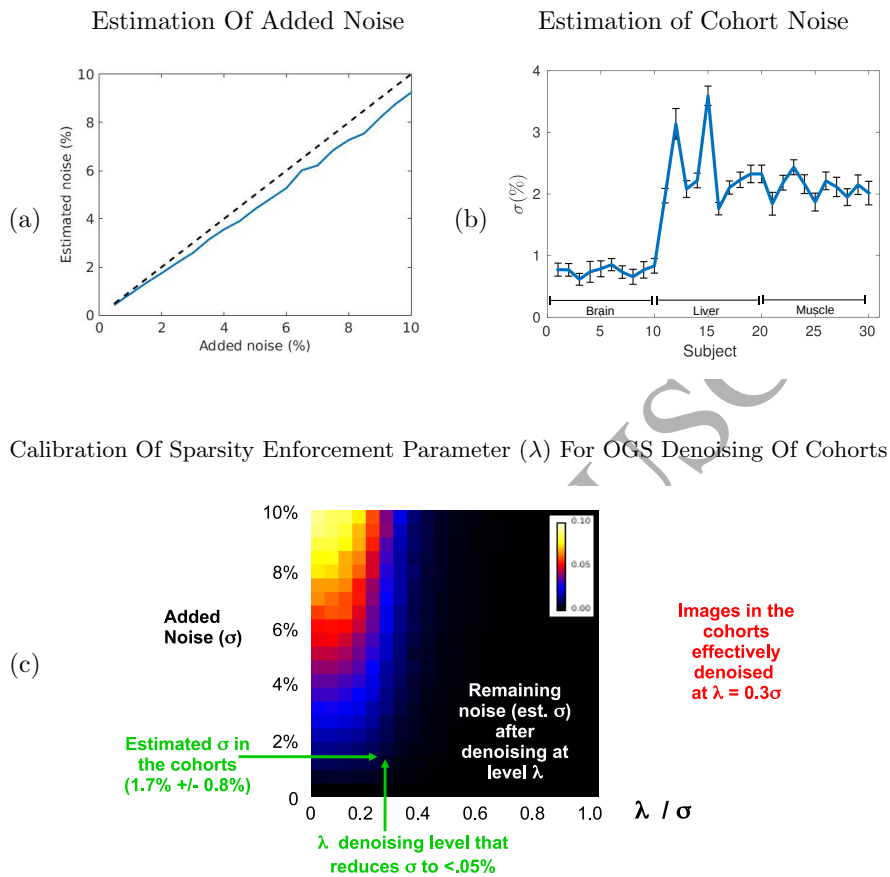λ denoising level that reduces σ to <.05%

Figure 2: Testing of noise estimators and denoising parameters. Panel (a) shows that the PCA-based noise estimation technique identifies added noise in an FEM MRE simulation to within $5.3\% \pm 2.6\%$ of prescribed. Panel (b) shows the same technique applied to the 30 cohorts in the study; estimated σ in the cohorts is $1.7 \pm 0.8\%$. Panel (c) compares different de-noising levels, in terms of OGS sparsity enforcement parameter λ, by estimating remaining noise after denoising with OGS. Added noise is reduced to $\sigma < 0.05\%$, at the levels of noise detected in the cohorts, when λ is set at 0.3σ.
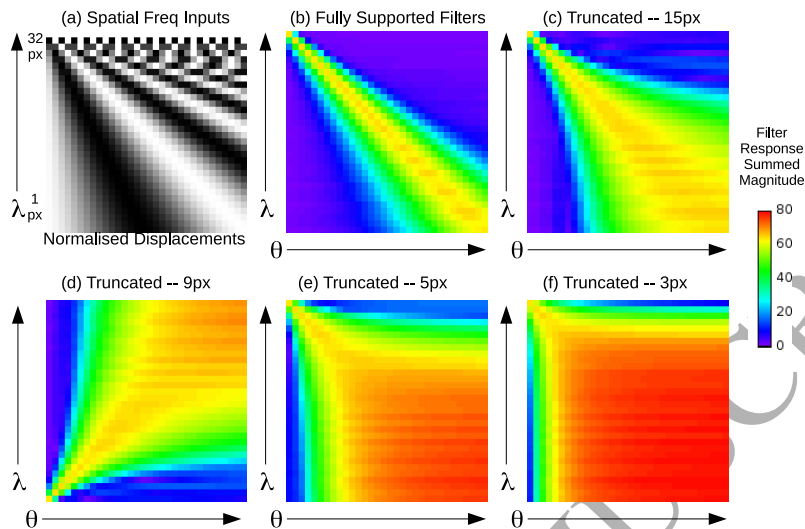
18

Figure 3: Reponse of truncated Gabor filters with tuning θ to spatial frequencies of wavelength λ. (a) shows the stack of 1D vectors at wavelengths (λ) = 1-32 px. All values are normalised 0 to 1. (b) shows the response of each Gabor filter tuning θ to each λ. Highest magnitude response is when $\theta = \lambda$. In panels (c-f), as the filters are truncated, they lose the ability to distinguish larger λ, but retain the capacity to distinguish some finer spatial frequencies even with compact support.
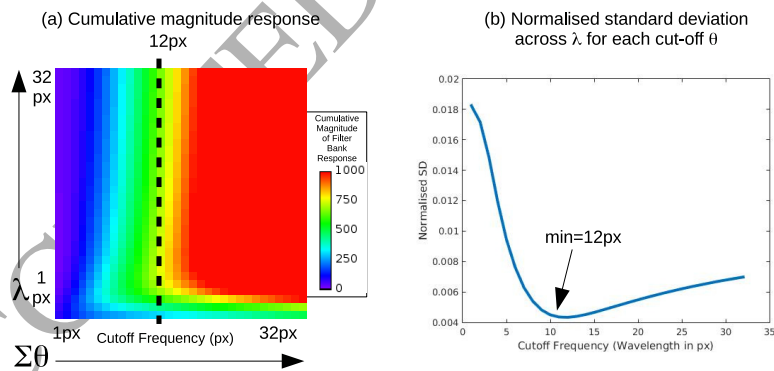

Figure 4: Cut-off for equal total frequency response for truncated Gabor bank. (a) Cumulative magnitude response for each λ was measured for each possible cutoff θ. (b) The filter bank with the most equal response across all λ (as measured by normalised SD) was chosen for the cut-off of the bank.

19

To visualise the filter's impact an illustration of the response of small and large truncated θ filters on a slice of brain MRE data is shown in Figure 5.

3.3. Simulation Noise Test

With the filter bank chosen, the FEM test data were processed with the ESP pipeline at the varying noise levels listed in Methods and compared to the MDEV pipeline. Figure 6 shows displacement and inversion images for the chosen noise levels for both MDEV and ESP. Figure 7 plots mean and standard deviation for hard target, soft target, and background material.

For MDEV $|G^*|$, noise-free estimates for hard target, soft target and background were 81%, 110% and 99% of prescribed respectively. The values decreased with increasing noise, such that in the 20% noise case, values were 33%, 72% and 60% of noise-free estimates respectively. For ESP $|G^*|$, noise-free estimates for hard target, soft target and background were 98%, 108% and 103% of noise-free estimates respectively. The values remained similar through the 20% noise case, with noise values 94%, 105%, and 99% of noise-free estimates respectively. Qualitatively, some artefacts can be seen. MDEV inversion retains shape of targets accurately, but ESP shows some shape distortion as noise level increases.

For MDEV ϕ, noise-free estimates for hard target, soft target and background were 620%, 109% and 110% of prescribed respectively. In the 20% noise case, values were 187%, 117% and 196% of noise-free estimates respectively. For ESP ϕ, noise-free estimates for hard target, soft target and background were 491%, 102% and 107% of noise-free estimates respectively. The values remained similar through the 20% noise case, with noise values 120%, 87%, and 101% of noise-free estimates respectively. Qualitatively, bright rings are seen in the ϕ values around the hard target. Noting that clinical liver MRE often uses manually drawn ROIs (Mariappan et al., 2010), a smaller region was drawn post-hoc in the hard target avoiding the artefactual rings. In the post-hoc ROI, estimates of hard target ϕ dropped to 247% for MDEV and 105% for ESP.

For visualisation of the impact of the denoising methods, Figure 8 illustrates

20

High frequency filter   Low frequency filter

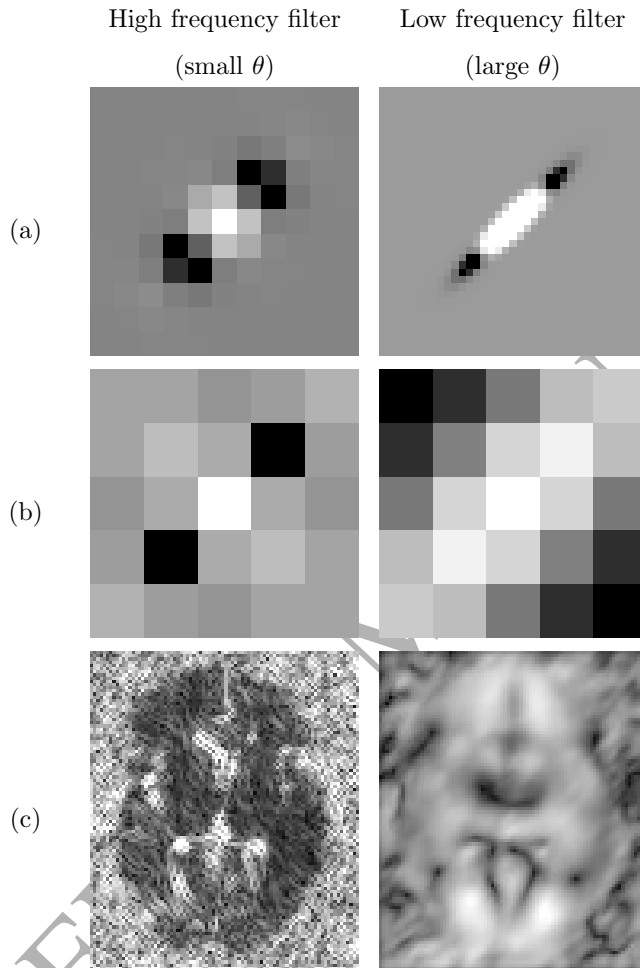(small θ)   (large θ)

(a)

(b)

(c)

Figure 5: Illustration of Gabor feature detection in *in vivo* samples. All filters, image volumes and convolutions are full 3D in the pipeline, and slices are shown only for demonstration. (a) Central slice of real component of 3D filter, yaw $\frac{\pi}{4}$, pitch 0, high and low spatial frequencies. (b) Truncation of filters to 5px compact support. (c) Magnitude of filter response in a slice of brain. The high-frequency filter responds to fine features, with brighter values at interfaces, and the low-frequency filter responds to coarse features, with brighter values at homogeneous tissue regions. Highest response is in the direction of the filter.
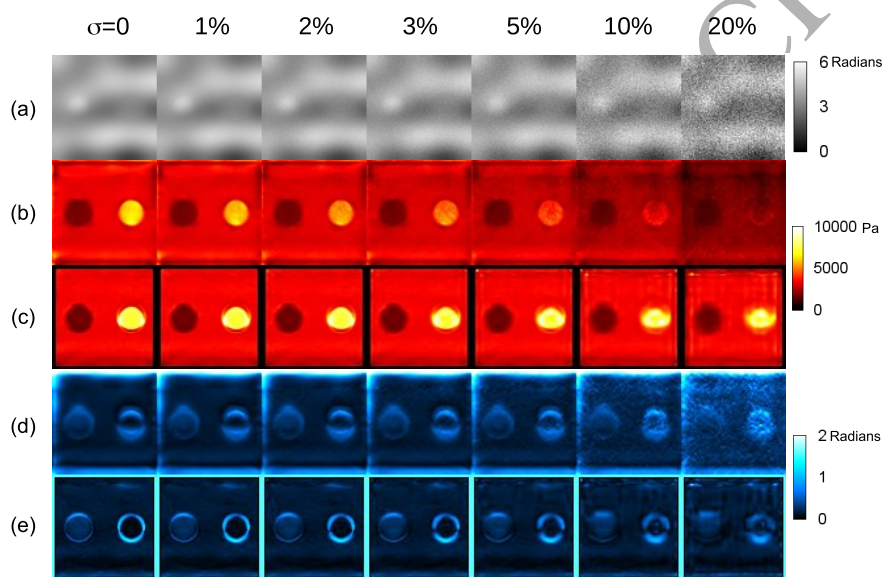
Figure 6: Images from the FEM noise test. (a) Z displacements of the simulation full vector field. (b), (c) Complex shear modulus magnitude $|G^*|$ from MDEV and ESP pipelines, respectively. (d), (e) Shear modulus phase angle ϕ from MDEV and ESP pipelines.
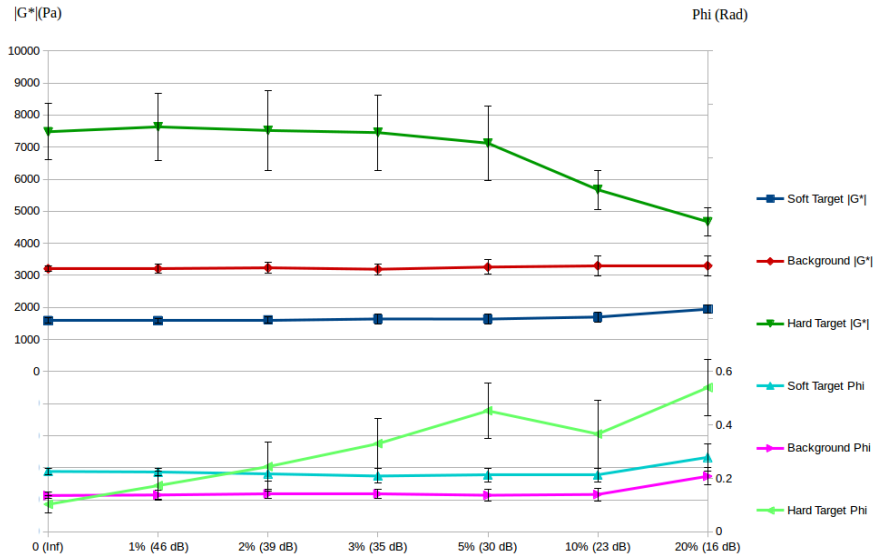
22

Figure 7: Plot of summary statistics for the FEM noise test. The MDEV pipeline shows sensitivity to noise while the ESP pipeline stays robust up to 20% noise.

the impact of the denoising methods using a detail measurement from an axial muscle acquisition.

3.4. In Vivo Cohorts: Comparison of MDEV and ESP images, and Comparison of MDEV, ESP, and LFE means.

Image comparisons of stiffness maps for the MDEV, and ESP pipelines are shown in Figure 9.

Means of each volume are plotted in Figure 11 and summary statistics are shown in Table 1 and Table 2. All three methods are significantly ($p < 0.01$) correlated in liver ($\mathbf{R} = 0.79, 0.88$ and 0.77). ESP and MDEV show a significant correlation ($p < 0.01$) in all cohorts but no significant correlations to LFE in brain or muscle. ESP showed consistently higher results than MDEV (16%, 55% and 32% for brain, liver, and thigh, respectively), while LFE did not show a consistent relationship to the values of the other two methods, being higher than both in brain, similar to ESP in liver, and lower than both in muscle.
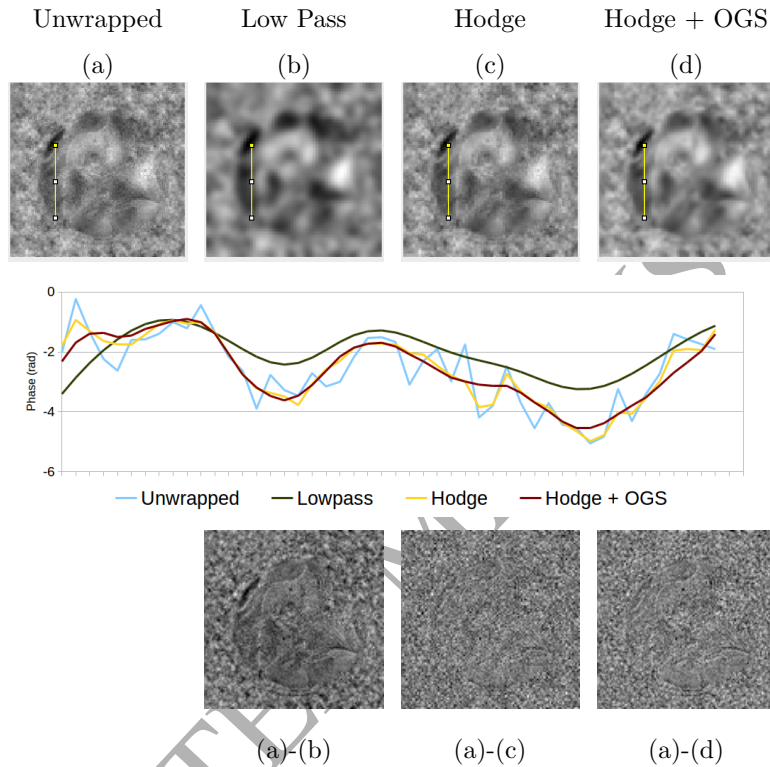
23

Unwrapped	Low Pass	Hodge	Hodge + OGS
(a)	(b)	(c)	(d)

(a)-(b)	(a)-(c)	(a)-(d)

Figure 8: Illustration of ESP denoising results on central slice of an axial thigh muscle acqusition. Images (a) is phase-unwrapped but not denoised. To compare with other image processing pipelines, (b) shows denoising results for a 4th order Butterworth low-pass filter with cutoff of 10mm. The remaining images show ESP methods. (c) shows the impact of the divergence-free wavelet. (d) shows the additional impact of the OGS denoising. To study the denoising results a vertical plot line was drawn across heterogeneous tissue features in the image. Comparison of the dark red and dark green lines shows the increase in detail from ESP's multiscale filtering (red) as opposed to low-pass filtering (green), even as both produce data sufficiently smoothed for wave inversion. Below the plot, subtraction images from (a) are shown for each de-noising step.
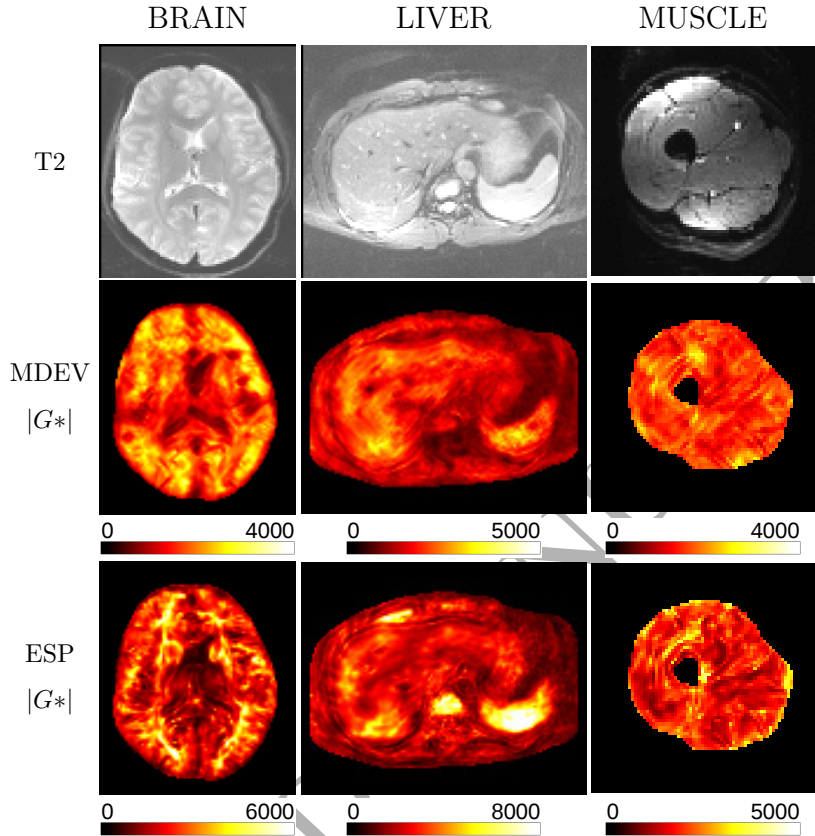
Figure 9: Comparison of $|G^*|$ and ϕ maps using the MDEV and ESP pipelines. All values are in Pascals.

Summary statistics for three-pipeline comparison

Mean / SD in Pascals

	BRAIN	LIVER	MUSCLE
LFE	3047 ± 338	2609 ± 501	916 ± 353
MDEV	1919 ± 184	1570 ± 216	1725 ± 85
ESP	2532 ± 448	2440 ± 313	2003 ± 164

Table 1: Means and standard deviations for each cohort by inversion method.
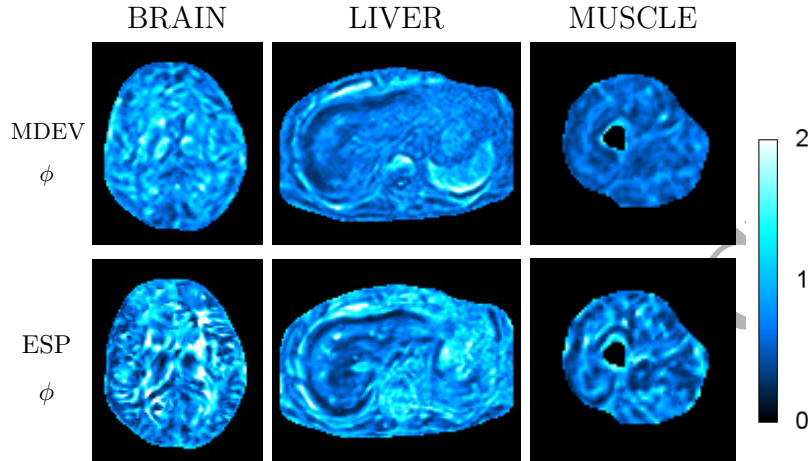
25

ϕ (ϕ) **Image Comparison**

Figure 10: Example images of viscoelasticity parameter ϕ (in Radians) for the same three organs as Figure 9 above.
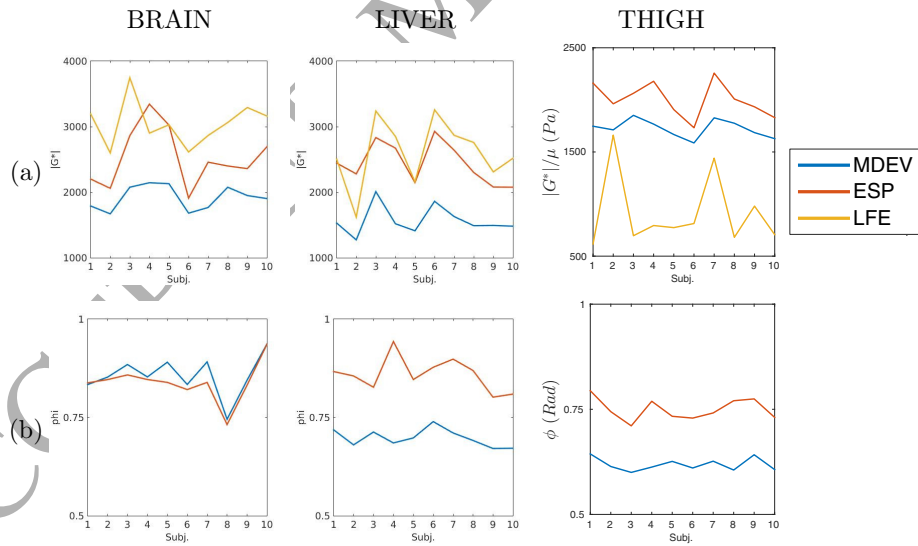

Figure 11: (a) Cross-pipeline comparison of mean stiffness values, μ for LFE and $|G^*|$ for MDEV and ESP, for each cohort. (b) Comparison of mean ϕ values for each volume as inverted by MDEV and ESP (LFE does not provide a ϕ image).

26

Correlations between pipeline results

	Stiffness			ϕ
	MDEV & ESP	MDEV & LFE	ESP & LFE	MDEV & ESP
Brain	**R**=0.85**	**R**=0.55	**R**=0.38	**R**=0.92***
Liver	0.79**	0.88***	0.77**	0.32
Thigh	0.85**	0.12	0.18	0.64*

Table 2: Correlations between results for the 3 inversion methods of LFE, MDEV and ESP (*=$p < 0.05$, **=$p < 0.01$, ***=$p < 0.001$). Results are significantly correlated in the liver cohort for all three methods, while ESP and MDEV $|G^*|$ are significantly correlated for all methods.

3.5. Reduced Energy Ratio (RER) Analysis

Results for the RER comparison of the ESP and MDEV pipelines are shown in Figure 12. Using a two-tailed t test, ESP significantly increases the RER for both the $|G^*|$ ($p < 1 \times 10^{-9}$) and ϕ ($p < 1 \times 10^{-3}$) maps.

4. Discussion

4.1. Noise and artefact in ESP and MDEV: FEM Results

The FEM testing suggests that fine features can indeed be recovered with ESP, even at SNR levels much lower than that found *in vivo*, but with some limitations. For $|G^*|$, the FEM hard target showed some spatial distortion while the ϕ targets showed artefactual rings, particularly around the hard target. Nonetheless, ESP recovered values within 8% of prescribed, at SNR levels substantially lower than that found *in vivo*, except in the case of hard target ϕ, and in this case, when the ROI was manually drawn rather than automatically chosen from the prescribed scheme, values also were within 5%.

In both cases of noticeable artefact – the hard target shape distortion in $|G^*|$ and the ring artefacts in ϕ – the ESP inversion of FEM simulation shows artefact that is asymmetric in the direction of wave motion, but symmetric in
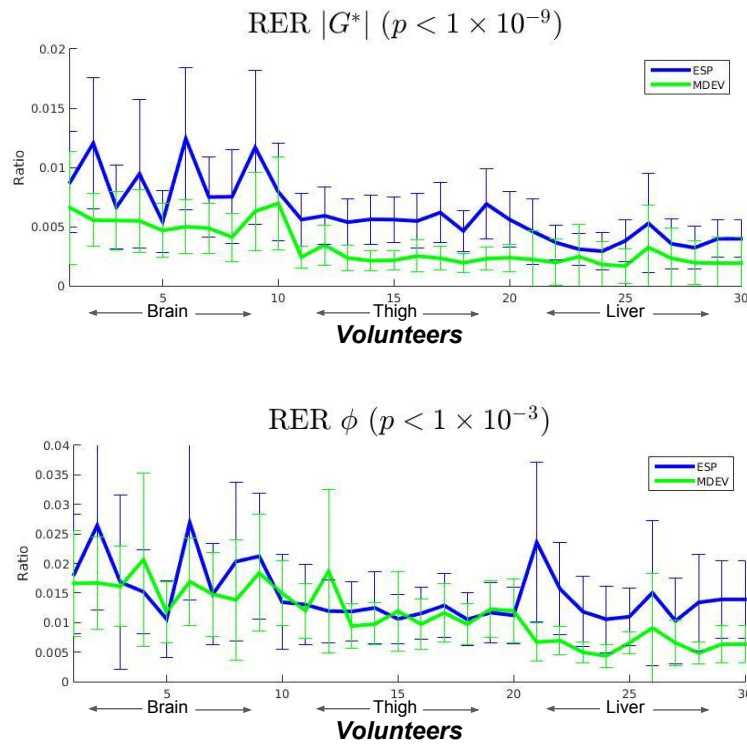
Figure 12: Reduced Energy Ratio (RER) comparison for ESP and MDEV pipelines. ESP shows a statistically significant increase in spectral energy at finer frequencies for both $|G^*|$ and ϕ.

the direction perpendicular to the motion. These artefacts are likely near-field scattering effects.

Differences between MDEV and ESP pipeline results can be explained by the differences between the filtering techniques in the pipelines. First, the underestimation of the hard target $|G^*|$ values by MDEV can be ascribed to loss of low-frequency bandwidth from the inversion of numerically estimated gradients, which have suppressed low-range frequency response. ESP, which inverts original displacements and uses a divergence-free-wavelet to remove bulk wave artefacts, retains these long wavelengths and measures the hard target more accurately. However, the 1mm resolution of the FEM simulation makes the hard target waves quite long, and wavelengths of this length are unlikely to be relevant *in vivo*. For expected wavelengths in, for example, 2mm voxels with tissue stiffness ranging up to $\approx 6400Pa$ (double the background value of the present study), using MDEV, only a slight underestimation would be expected, and only at the high end of that stiffness range.

In $|G^*|$, MDEV does not show ESP's shape distortion around the hard target. This is likely a benefit of the MDEV pipeline's band-pass approach, in which the fine spatial frequencies from the scattering are well suppressed by the Butterworth filter, leaving only spatial frequencies that correspond to propagation rather than scattering. As ESP retains information along the entire available frequency spectrum, it may be susceptible to scattering from hard areas within a volume. However, no such shape distortion is shown between the soft target and background material in ESP, suggesting that, as discussed for MDEV above, under the conditions and stiffness levels present in *in vivo* MRE, this is unlikely to be a concern. This conclusion was supported further by qualitiative inspection of the *in vivo* images, which showed good spatial correspondence between elastogram features and features as seen on a T2 image.

4.2. Details And Values In Three Inversion Pipelines: In Vivo Results

For $|G^*|$ *in vivo*, ESP and MDEV showed good correlation. While both methods use the same inversion equations, they use entirely different filtering

29

and phase unwrapping techniques, and the correlation between images suggests that both denoising methods deliver accurate assessment of the relative viscoelastic properties of anatomical structures.

In ϕ, results were mixed, with high $\mathbf{R}$ for brain, low $\mathbf{R}$ for liver and moderate $\mathbf{R}$ for thigh. Inspection of the ϕ maps in Figure 10 suggests that as ESP picks up more details, it gains high scatter-related values, increasing and decorrelating the results from those of the MDEV pipeline.

The close correlation between ESP and LFE in liver was striking, and a further validation of the utility of MRE for liver stiffness measurement. MDEV correlated to both but remained at lower values. What ESP and LFE share, that MDEV does not, is the use of multiple scales in the inversion (Knutsson et al., 1994). As MDEV uses only a compact-windowed Laplacian operator, this may explain its slightly lower values.

One weakness in this analysis is that LFE contains many manual settings, which were left to defaults when possible. It is possible that tuning of the setting for each cohort, and indeed for each image, may have produced more correlated results in all three pipelines. LFE did not show high correlation values with ESP or MDEV in brain or thigh. This may relate to the default 2D approach of LFE, particularly in brain where waves are highly reverberant in all three dimensions. Similar concerns may pertain to muscle although other 2D approaches to axial thigh images have produced similar values to this study (Klatt et al., 2010; Barnhill, 2013; Guo et al., 2015). Overall, such operator-dependent choices are difficult to objectify and consequently we use the means from default LFE results for a benchmark comparison only.

The RER quantifies a statistically significant increase in fine frequency spectral energy found in ESP images as compared with MDEV. The requirement of $8 \times 8 \times 8$ blocks created variance at sharp boundaries so that some regions of anatomy were excluded. However the finding of increased fine frequency activity in ESP was highly robust and the measurement was likely not confounded by this. The statistical significance was lower in the ϕ map and this can be attributed to the increasing image noise resulting from ϕ scattering.

30

Results from all three pipelines are available on request to interested researchers for further inspection, and a copy of the ESP pipeline as Matlab code can be obtained by contacting CRIC at the University of Edinburgh.

4.3. Sparsification and Phase Noise

Here our calibration of sparsity enforcement parameter λ resulted in reduction of estimated noise levels to $\leq 0.05\%$. This is higher than the results for speech denoising reported in Chen and Selesnick (2014), in which noisy signals are reduced to noise levels of $\sigma = 3 \times 10^{-4}$. However, the above-mentioned improvement in RER suggests that this denoising takes place without loss of fine feature information, but rather improves its retention as compared to MDEV, and is therefore sufficient in the MRE context.

SNR is likely to change across the image in relation to wave amplitude, with SNR decreasing as the wave amplitude decreases from damping. The independent sparsification of each overlapping group is expected to be responsive to this variance, however, the de-noising for each slice is still calibrated to a single SNR value, and future work will address this limitation. As the FEM simulation used uniform noise parameters for each image, they did not address this issue directly, though it is noteworthy that ESP remained robust through a wide range of noise without changing any settings. As each overlapping group is de-noised independently one likely avenue for future work is the use of an SNR map of the image to adaptively determine λ of each individual group.

5. Conclusion

ESP holds promise as a software tool for fine-featured MRE images. The chief goal of ESP was the inversion of MRE data while preserving the complete bandwidth of the image. This required denoising in wavelet bases using nonlinear thresholding techniques, combination of results at multiple frequencies, and the incorporation of Gabor-based feature detection to invert features at their appropriate scales. The new pipeline produced a significant increase in Reduced Energy Ratio (RER) for both viscoelastic parameters, suggesting better

31

retention of the fine range of spatial frequencies, though FEM testing showed that some of the fine-frequency information may be scattering or inhomogeneity artefact. Also FEM testing showed more accurate measurement than MDEV with coarse spatial frequencies, suggesting that the techniques incorporated into ESP improve spatial frequency estimation at both ends of the spectrum.

The combination of FEM and RER results suggest that at the estimated noise levels of *in vivo* cohorts of brain, abdomen or thigh muscle, ESP can be expected to retain fine features and wider stiffness contrasts, while removing noise and clutter from known MRE noise sources, and this assertion is supported by qualitative inspection of *in vivo* results. Further, ESP shows overall good correlation with the related MDEV pipeline, and in liver produces results similar in value to the 2D LFE inversion method.

Acknowledgements

32

Vitae

Eric Barnhill Eric Barnhill is a PhD candidate in Medical Physics at the
Clinical Research Imaging Centre (CRIC), University of Edinburgh, spe-
cialising in MRE post-processing and computation. He is the recipient
of the SUPA Industrial Studentship Prize, a SINAPSE (Scottish Imag-
ing Network) Career Development Grant, and a University of Edinburgh
Department of Informatics / UK Medical Research Council Confidence in
Concept Post-Doctoral Fellowship.

Lyam Hollis Lyam Hollis graduated from Lancaster in 2011 with an under-
graduate masters in Physics, Astrophysics and Cosmology before under-
taking a masters in Cardiovascular Biology at the University of Edinburgh.
Lyam is currently reading for his PhD at Edinburgh specialising in finite
element modelling of magnetic resonance elastography.

Ingolf Sack Ingolf Sack graduated as a chemist at Technical University of
Berlin, did his PhD in NMR spectroscopy at Free University of Berlin
and was a postdoc working in the fields of solid state NMR, MRI and
Elastography at the Weizmann Institute in Israel, the University Hospital
Benjamin Franklin in Berlin and the Sunnybrook Hospital of University
of Toronto. Since 2004 he leads a research group at the Charité Hospital
Berlin which is focused on method developments in elasticity-based imag-
ing by MRI and sonography. Since 2010 he is a full professor within the
Heisenberg program of the German Research Foundation.

Jürgen Braun Dr. Jürgen Braun is currently associate professor in Medical
Informatics at Charité - Universittsmedizin Berlin. He earned his PhD in
Physical Chemistry from the University of Freiburg in 1994. Since 2001 he
is Co-PI of the elastography group of the Charité. He is a worldwide lead-
ing developer of MRE sequences and hardware and he also pioneered time
harmonic ultrasound elastography. His expertise in mechanical engineer-
ing and MRI has facilitated many clinical applications of MRE including

33

that of neurological disorders, cardio MRE and MRE of the liver. He has over 90 refereed publications, several awards, 2 granted and 7 pending patents.

Peter R Hoskins Prof. Peter Hoskins studied Physics at Oxford University graduating in 1980. He has been in Edinburgh for 30 years initially as a Hospital Physicist in the National Health Service where he became Consultant Physicist in 1998. He moved to Edinburgh University in 2006 and is currently Professor of Medical Physics and Biomechanics. He was awarded a PhD in 1990 for work on obstetric ultrasound and DSc in 2009 for work on arterial mechanics. Research interests include development of ultrasound techniques for diagnosis of cardiovascular disease, patient specific modelling and elastography. He has published 120 refereed journal papers and is principal author of 3 books.

Pankaj Pankaj Dr. Pankaj Pankaj is a Reader in computational biomechanics at the University of Edinburgh. He obtained his PhD in numerical modelling from University of Wales Swansea. At Edinburgh he leads the Orthopaedic Biomechanics research group and has research collaborations with universities in Europe, Asia, South America and Australia. Research supervised by him has received a number of recent awards: Robertson Medal from the Carnegie Trust; IMechE award for the best medical engineering PhD; and Vicon award for the best medical engineering project.

Colin Brown Colin Brown has worked for 30 uninterrupted years in the pharmaceutical & consumer healthcare industries. As a chemist, he has held several positions in the pharmaceutical development, clinical trials supplies and research & development of medicinal products across a range of therapeutic areas and pharmaceutical forms. Having begun his career at Syntex Pharmaceuticals before moving to Quintiles, a Contract Research Organisation in Edinburgh, he is currently Director of Research & Quality Development at Mentholatum's European headquarters in Scotland where

34

he is responsible for the R&D, regulatory affairs, pharmacovigilance and quality of the company's activities in Europe, Middle East and Africa.

Edwin van Beek Prof van Beek is a graduate from Erasmus University Medical school, did his PhD and Radiology and Clinical Epidemiology training at Academic Medical Centre, University of Amsterdam, and subsequently spent 5 years at University of Sheffield, UK and nearly 6 years at University of Iowa, USA. In 2009, he took up the SINAPSE Chair of Clinical Radiology and co-directorship of the Clinical Research Imaging Centre, University of Edinburgh.

He has published extensively in the field of cardiothoracic and molecular imaging, and was particularly involved in multidisciplinary research including medical physics and biomedical engineering applications in the field of diagnostic imaging.

Neil Roberts Between 1988 and 2008 Prof. Roberts led a research programme entitled "Magnetic Resonance Studies of the Neural Bases of Cognition: Theoretical and Clinical Interactions" at the University of Liverpool where he was Director of the Magnetic Resonance and Image Analysis Research Centre (MARIARC). During this time Neil was a Principal Investigator on two Medical Research Council (MRC) Programme Grants concerning the study of the neural bases of memory and language, providing expertise in Magnetic Resonance Imaging (MRI) and Image Analysis. In 2009 Neil was appointed Chair of Medical Physics and Imaging Science at the University of Edinburgh and has established a new research programme in Magnetic Resonance Elastography.

References

Aharon, M., Elad, M., Bruckstein, A., 2006. K-svd: An algorithm for designing overcomplete dictionaries for sparse representation. Signal Processing, IEEE Transactions on 54 (11), 4311–4322.

Aster, R. C., Borchers, B., Thurber, C. H., 2013. Parameter estimation and inverse problems. Academic Press.

Barnhill, E., 2013. Neural connectivity, music, and movement: A response to pat amos. Frontiers in Integrative Neuroscience 7 (29).

Barnhill, E., Kennedy, P., Hammer, S., van Beek, E. J., Brown, C., Roberts, N., 2013. Statistical mapping of the effect of knee extension on thigh muscle viscoelastic properties using magnetic resonance elastography. Physiological measurement 34 (12), 1675.

Barnhill, E., Kennedy, P., Johnson, C. L., Mada, M., Roberts, N., 2014. Real-time 4d phase unwrapping applied to magnetic resonance elastography. Magnetic Resonance in Medicine.

Bensamoun, S. F., Ringleb, S. I., Chen, Q., Ehman, R. L., An, K.-N., Brennan, M., 2007. Thigh muscle stiffness assessed with magnetic resonance elastography in hyperthyroid patients before and after medical treatment. Journal of Magnetic Resonance Imaging 26 (3), 708–713.

Bertero, M., Boccacci, P., 2010. Introduction to inverse problems in imaging. Taylor & Francis.

Braun, J., Guo, J., Lützkendorf, R., Stadler, J., Papazoglou, S., Hirsch, S., Sack, I., Bernarding, J., 2013. High-resolution mechanical imaging of the human brain by three-dimensional multifrequency magnetic resonance elastography at 7t. NeuroImage.

Chen, P.-Y., Selesnick, I. W., 2014. Group-sparse signal denoising: non-convex regularization, convex optimization. Signal Processing, IEEE Transactions on 62 (13), 3464–3478.

Clausi, D. A., Jernigan, M. E., 2000. Designing gabor filters for optimal texture separability. Pattern Recognition 33 (11), 1835–1849.

Dabov, K., Foi, A., Katkovnik, V., Egiazarian, K., 2009. Bm3d image denoising with shape-adaptive principal component analysis. In: SPARS'09-Signal Processing with Adaptive Sparse Structured Representations.

Donoho, D. L., Johnstone, I. M., 1995. Adapting to unknown smoothness via wavelet shrinkage. Journal of the american statistical association 90 (432), 1200–1224.

Gonzalez, R., Woods, R. E., 2002. Digital image processing. Prentice Hall Press, ISBN 0-201-18075-8.

Green, M., Bilston, L., Sinkus, R., 2008. In vivo brain viscoelastic properties measured by magnetic resonance elastography. NMR in Biomedicine 21 (7), 755–764.

Guo, J., Hirsch, S., Fehlner, A., Papazoglou, S., Scheel, M., Braun, J., Sack, I., 2013. Towards an elastographic atlas of brain anatomy. PloS one 8 (8), e71807.

Guo, J., Hirsch, S., Scheel, M., Braun, J., Sack, I., 2015. Three-parameter shear wave inversion in mr elastography of incompressible transverse isotropic media: Application to in vivo lower leg muscles. Magnetic Resonance in Medicine.

Guo, J., Hirsch, S., Streitberger, K., Kamphues, C., Asbach, P., Braun, J., Sack, I., 2014. Patient-activated three-dimensional multifrequency magnetic resonance elastography for high-resolution mechanical imaging of the liver and spleen. RoFo: Fortschritte auf dem Gebiete der Rontgenstrahlen und der Nuklearmedizin 186 (3), 260–266.

Hirsch, S., Guo, J., Reiter, R., Papazoglou, S., Kroencke, T., Braun, J., Sack, I., 2014. Mr elastography of the liver and the spleen using a piezoelectric driver, single-shot wave-field acquisition, and multifrequency dual parameter reconstruction. Magnetic Resonance in Medicine 71 (1), 267–277.

Honarvar, M., Sahebjavaher, R., Salcudean, S., Rohling, R., 2012. Sparsity regularization in dynamic elastography. Physics in medicine and biology 57 (19), 5909.

Honarvar, M., Sahebjavaher, R., Sinkus, R., Rohling, R., Salcudean, S., 2013. Curl-based finite element reconstruction of the shear modulus without assuming local homogeneity: Time harsdddmonic case.

Klatt, D., Hamhaber, U., Asbach, P., Braun, J., Sack, I., 2007. Noninvasive assessment of the rheological behavior of human organs using multifrequency MR elastography: a study of brain and liver viscoelasticity. Physics in medicine and biology 52, 7281.

Klatt, D., Papazoglou, S., Braun, J., Sack, I., 2010. Viscoelasticity-based MR elastography of skeletal muscle. Physics in Medicine and Biology 55 (21), 6445.

Knutsson, H., Westin, C.-F., Granlund, G., 1994. Local multiscale frequency and bandwidth estimation. In: Image Processing, 1994. Proceedings. ICIP-94., IEEE International Conference. Vol. 1. IEEE, pp. 36–40.

Lee, S.-Y., Yoo, J.-T., Kumar, Y., Kim, S.-W., 2009. Reduced energy-ratio measure for robust autofocusing in digital camera. Signal Processing Letters, IEEE 16 (2), 133–136.

Liu, X., Tanaka, M., Okutomi, M., 2013. Single-image noise level estimation for blind denoising. Image Processing, IEEE Transactions on 22 (12), 5226–5237.

Malkin, A. Y., Isayev, A. I., 2006. Rheology: concepts, methods, and applications. ChemTec Publishing.

Manduca, A., Lake, D. S., Kruse, S., Ehman, R. L., 2003. Spatio-temporal directional filtering for improved inversion of mr elastography images. Medical image analysis 7 (4), 465–473.

Manduca, A., Oliphant, T., Dresner, M., Mahowald, J., Kruse, S., Amromin, E., Felmlee, J., Greenleaf, J., Ehman, R., 2001. Magnetic resonance elastography: non-invasive mapping of tissue elasticity. Medical Image Analysis 5 (4), 237–254.

Mariappan, Y. K., Glaser, K. J., Ehman, R. L., 2010. Magnetic Resonance Elastography: A Review. Clinical Anatomy 23, 497–511.

McGarry, M. D., 2013. Improvement and evaluation of nonlinear inversion MR elastography. Dartmouth College.

Murphy, M. C., Huston, J., Glaser, K., Manduca, A., Felmlee, J., Ehman, R., 2012. Phase correction for interslice discontinuities in multislice epi mr elastography. In: Proceedings of the 20th ISMRM Annual Meeting. No. 3426. ISMRM.

Muthupillai, R., Lomas, D. J., Rossman, P. J., Greenleaf, J. F., Manduca, A., Ehman, R. L., Sep. 1995. Magnetic Resonance Elastography by Direct Visualization of Propagating Acoustic Strain Waves. Science 269 (5232), 1854–1857.

Ong, F., Uecker, M., Tariq, U., Hsiao, A., Alley, M. T., Vasanawala, S. S., Lustig, M., 2014. Robust 4d flow denoising using divergence-free wavelet transform. Magnetic Resonance in Medicine.

Papazoglou, S., Braun, J., Hamhaber, U., Sack, I., 2005. Two-dimensional waveform analysis in mr elastography of skeletal muscles. Physics in Medicine and Biology 50 (6), 1313.

Papazoglou, S., Hirsch, S., Braun, J., Sack, I., 2012. Multifrequency inversion in magnetic resonance elastography. Physics in medicine and biology 57 (8), 2329.

Park, E., Maniatty, A. M., 2006. Shear modulus reconstruction in dynamic elastography: time harmonic case. Physics in medicine and biology 51 (15), 3697.

Sack, I., Jöhrens, K., Würfel, J., Braun, J., 2013. Structure-sensitive elastography: on the viscoelastic powerlaw behavior of in vivo human tissue in health and disease. Soft Matter 9 (24), 5672–5680.

Selesnick, I. W., Baraniuk, R. G., Kingsbury, N. C., 2005. The dual-tree complex wavelet transform. Signal Processing Magazine, IEEE 22 (6), 123–151.

Sinkus, R., Lorenzen, J., Schrader, D., Lorenzen, M., Dargatz, M., Holz, D., 2000. High-resolution tensor mr elastography for breast tumour detection. Physics in medicine and biology 45 (6), 1649.

Sinkus, R., Tanter, M., Catheline, S., Lorenzen, J., Kuhl, C., Sondermann, E., Fink, M., 2005a. Imaging anisotropic and viscous properties of breast tissue by magnetic resonance-elastography. Magnetic resonance in medicine 53 (2), 372–387.

Sinkus, R., Tanter, M., Catheline, S., Lorenzen, J., Kuhl, C., Sondermann, E., Fink, M., 2005b. Imaging anisotropic and viscous properties of breast tissue by magnetic resonance-elastography. Magnetic Resonance in Medicine 53 (2), 372–387.

Streitberger, K.-J., Reiss-Zimmermann, M., Freimann, F. B., Bayerl, S., Guo, J., Arlt, F., Wuerfel, J., Braun, J., Hoffmann, K.-T., Sack, I., 2014. High-resolution mechanical imaging of glioblastoma by multifrequency magnetic resonance elastography. PloS one 9 (10), e110588.

Szabo, T. L., 1995. Causal theories and data for acoustic attenuation obeying a frequency power law. The Journal of the Acoustical Society of America 97, 14.

Thomas-Seale, L. E. J., Klatt, D., Pankaj, P., Roberts, N., Sack, I., Hoskins, P. R., 2011. A simulation of the magnetic resonance elastography steady state wave response through idealised atherosclerotic plaques. IAENG International Journal of Computer Science 38 (4), 394 – 400.